Supplemental Material: Temporal light control in complex media through the singular value decomposition of the time-gated transmission matrix

Louisiane Devaud,[1,*] Bernhard Rauer,[1] Matthias Kühmayer,[2]
Jakob Melchard,[2] Mickaël Mounaix,[1,3] Stefan Rotter,[2] and Sylvain Gigan[1]

[1] *Laboratoire Kastler Brossel, ENS-Université PSL, CNRS, Sorbonne Université, Collège de France, 24 rue Lhomond, 75005 Paris, France*
[2] *Institute for Theoretical Physics, Vienna University of Technology (TU Wien), A-1040 Vienna, Austria*
[3] *School of Information Technology and Electrical Engineering, The University of Queensland, Brisbane, QLD 4072, Australia*

(Dated: April 20, 2022)

I. FIELD MEASUREMENT: DELAY LINE SCAN VS. HOLOGRAPHY

We use two techniques to extract the field of the scattered light. The first relies on standard digital phase-stepping holography. For this the delay line is fixed to the desired delay time of the probe pulse. We then globally modulate the phase with the SLM (phase-stepping) and record the interference pattern between the scattered light and the plane wave probe pulse on the CCD. From the different images recorded we retrieve the field of the scattered light. We employ this technique to measure the transmission matrix as well as to retrieve the field for given fixed delays. This technique is fast and especially useful for repeated measurement to allow for averaging.

The second technique relies on interferometric cross-correlation [1], which retrieves the entire temporal evolution of the scattered light within the pulse. It can be seen as a continuous version of the phase-stepping holography described above. Here the SLM displays a fixed pattern and the phase modulation is realised by tuning the delay line. The delayed probe pulse is scanned over the broad scattered pulse while the CCD continuously records the resulting intereferogram. Looking at a single pixel, the main frequency of the recorded signal is the carrier frequency of the laser. Fourier filtering to extract just the amplitude of this oscillation returns the local pulse shape of the scattered light impinging on this pixel. All temporal data presented in this article is measured in this way. Compared to the first technique, this method is however quite slow such that in situations where repeated measurements are necessary, it becomes impractical.

II. DEFINITION OF THE TEMPORAL ORIGIN

For the measured temporal data presented in Fig. 2 as well as Fig. 4(b) of the main text, the time $\tau = 0$ is defined to correspond to the delay line position δx at which the two arms of the interferometer have the same optical path length in presence of the scattering medium. To determine this point we use quasi-monochromatic light (pulse width of $\Delta\lambda < 0.1\,\mathrm{nm}$) whose wavelength we tune continuously over a scale of $\pm 3\,\mathrm{nm}$ around $\lambda_0 = 808\,\mathrm{nm}$. In the case of a non-zero path length difference $|\delta x| > 0$, different wavelengths will pick up different relative phases over δx. When tuning the wavelength, this leads to an oscillation of the global phase of the field measured with the phase-stepping holography technique described above. The frequency of this oscillation depends linearly on the path length difference and goes to zero when the two paths are of equal length. We probe these oscillations by calculating the correlations between the measured λ-dependent field and the field measured at λ_0. Doing this for different delay line positions δx we obtain the pattern shown in Fig. S1(a). A clear symmetry point is observed when the path length difference, and with it the oscillation frequency, goes to zero. Fourier transforming the oscillations along λ allows to determine $\delta x = 0$, defining the temporal origin (Fig. S1(b)).

For the simulations presented in Fig. 3 of the main text, the point $\tau = 0$ is defined as the time at which an input pulse would reach the output surface if the scattering region would be homogeneously filled with an averaged refractive index medium. The propagation delay can be computed from the mean group velocity of the excited modes, see Sec. V.

Note that the experimental method for determining $\delta x = 0$ is just an operational definition. Also for monochromatic light a distribution of different path length through the medium exists which leads to the pulse shape affecting the observed oscillations. However, we found that in practice this definition corresponds well with the temporal origin

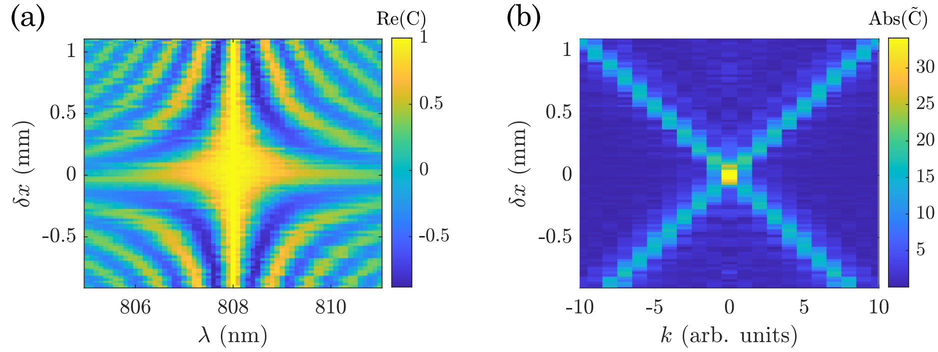

FIG. S1. Measurement of the point of equal path length. (a) Real part of the correlation C between the field speckle pattern obtained for a random input at wavelength λ with the respective reference pattern at $\lambda_0 = 808\,\mathrm{nm}$ for different lengths of the delay line δx. The fading of the pattern wavelength far from λ_0 results from the limited spectral decorrelation length of the medium. (b) Fourier transform $\tilde{C}$ along λ of the data presented in (a). The crossing point of the oscillation peaks is used to determine $\delta x = 0$.

of the simulations. In the end, the location of the temporal origin is arbitrary and does not play a role in the interpretation of the data.

III. DEFINITIONS OF CHARACTERISTIC QUANTITIES

A. Definition of γ

The amount of control in the experiment is defined by the parameter γ. It is given by

$$\gamma \equiv \frac{N_{\mathrm{out}}}{N_{\mathrm{in}}} \approx \frac{N_{\mathrm{CCD}}}{N_{\mathrm{SLM}}}, \tag{S1}$$

where N_{SLM} is the number of modes controlled on the SLM and N_{CCD} the number of pixels in the region of interest (ROI) of the camera. When measuring a TM the camera pixels are binned such that one pixel corresponds to one speckle grain. The typical numbers of targeted modes used in this article are $N_{\mathrm{SLM}}^{\mathrm{target}} = 32^2$ ($N_{\mathrm{SLM}}^{\mathrm{target}} = 16^2$ and $N_{\mathrm{SLM}}^{\mathrm{target}} = 62^2$ are used as well). However, due to geometric experimental limitations, i.e., the back focal plane of the illumination microscope objective cutting some SLM modes, the effective number of controlled modes needs to be estimated. This is done using the information contained in the TM. Taking the square root of the sum over the CCD dimension of the Hadamard product of the TM with its conjugate gives a vector that contains the information on the contribution of each SLM mode. Let us denote P the vector containing the information, one has

$$P_j = \sqrt{\sum_i (T \cdot T^*)_{i,j}} = \sqrt{\sum_i T_{i,j} \times T_{i,j}^*}, \tag{S2}$$

with $(A \cdot B)$ being the Hadamard product of two matrices A and B with equal dimensions. The vector P can be reshaped to visualise the SLM modes as presented in Fig. S2(a). Applying a threshold and summing the number of modes above this threshold enables to obtain an estimate of the effective value of N_{SLM} (see Fig. S2(b)).

The ROI on the camera is usually chosen large enough that we obtain smooth averaged pulse shapes while still being small enough that the probe pulse is sufficiently homogeneous over the whole area. In most experiments we work with $\gamma = 0.2$-0.3. The speckle grain size is extracted by taking the half width at half maximum of the cross-correlation of the field. To be insensitive to the sampling of the speckles this width is extracted by a Gaussian fit. The speckle grain size can also be extrapolated from the TM measurement [2]. It is given by the inverse of the participation number normalized by the rank of the TM.

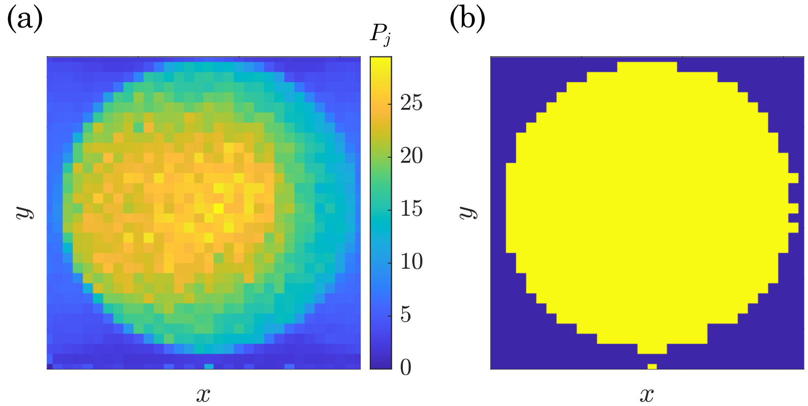

FIG. S2. Effective number of SLM modes. (a) Image of the SLM modes contribution to the TM obtained by reshaping the vector P obtained from Eq. (S2). (b) A threshold is applied and the number of effective modes computed by summing the modes above the threshold (fixed at 12 here). For the data in Fig. 2(a) of the main text, this results in $N_{\mathrm{SLM}} \approx 640$ modes effectively launched to measure the TM.

B. Definition of the normalized singular values

To observe the Marchenko-Pastur law in the distribution of singular values of a TM they need to be normalized. For a matrix of size $m \times n$ and singular values s_i this normalization is usually defined as

$$\tilde{s}_i^{\mathrm{MP}} = \frac{s_i}{\sqrt{\frac{1}{\min(n,m)} \sum_{j=1}^{\min(n,m)} s_i^2}}, \tag{S3}$$

regardless of the respective values of m and n. In physics normalizing the singular values of a TM such that they follow the Marchenko-Pastur law is often interesting [3]. However for a TM m and n have a physical meaning: the number of controlled modes (N_{SLM}) and the degrees of freedom (N_{CCD}). They no longer are interchangeable. To compute the mean over the singular values, all singular values equal to 0 should be included as they bring information on the transmission. Here we hence will use an alternative version of the normalized singular values to be able to link them to the enhancement. We define

$$\tilde{s}_i = \frac{s_i}{\sqrt{\frac{1}{N_{\mathrm{SLM}}} \sum_{j=1}^{N_{\mathrm{SLM}}} s_i^2}}. \tag{S4}$$

It is noteworthy that for $N_{\mathrm{SLM}} > N_{\mathrm{CCD}}$ (our experimental case), one has $\tilde{s}_i = \tilde{s}_i^{\mathrm{MP}}/\sqrt{\gamma}$.

IV. PEAK WIDTH AND TEMPORAL SHIFT OF THE PULSE MODULATION

In the main text we show that the SVD of the time-gated TM allows us to modulate the transmitted amplitude at any given point in the pulse (see Fig. 2(c)). However we do not discuss the width of the enhancement peaks. As visible in Fig. 2(a), the full width at half maximum of the amplitude peak is of 200 fs, broader than the initial pulse. The 100 fs width of the original pulse is the intensity width, the amplitude width of the original pulse is a factor of $\sqrt{2}$ larger. To this apparent broadening adds the homodyne measurement process. As we measure the scattered light by interfering it with the unperturbed probe pulse the obtained temporal evolution is given by a convolution of the two. Convolving two Gaussians of width σ leads to a Gaussian of width 2σ which accounts for the rest of the observed broadening.

Now we want to point out that for early and late times the targeted enhancement (or reduction) does not appear exactly at the desired time, as shown in Figs. S3(a) and (b). A way to understand this behaviour is to recall how the TM measurement is performed. The probe pulse interferes with the elongated one at the chosen time τ_0. The probe pulse width is the one of the non-elongated pulse (full width at hall maximum 100 fs) so that the measurement is not temporally sharp but is multiplied by the Gaussian envelope of the probe. There is then a temporal "freedom" for the peak position around the position τ_0. This explains the peak shifts to times at which it is easier to increase energy (i.e., where the field amplitude is higher). This temporal position mismatch is taken into account in the enhancement value extraction: the enhancement is measured at the peak position instead of τ_0.

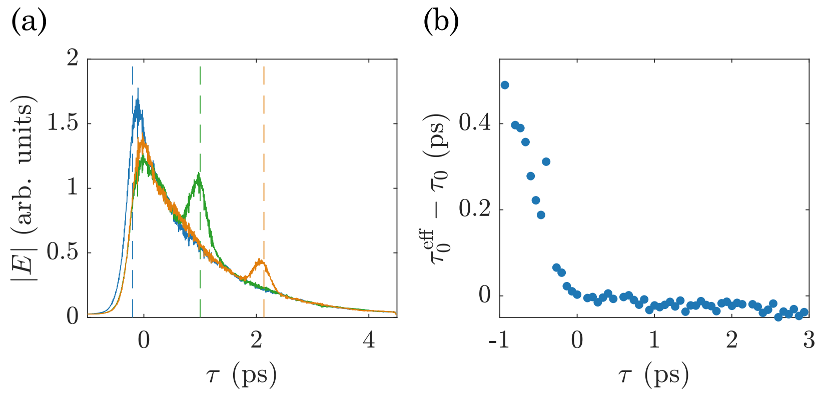

FIG. S3. Evolution of the peak position over the pulse. (a) Pulse shape of the first SVD states v_1 for different values of τ_0. It is possible to control energy delivery at all times within the distribution of delays induced by the scattering, but the peak positions do not exactly coincide with the chosen values of τ_0 (indicated by the vertical dashed lines). At early times (in the pulse peak rise, blue curve) the increase is shifted to the later times, whereas at later times (pulse tail, orange curve) the peak is shifted to the earlier times. In both cases this corresponds to a shift in direction of the higher field. For intermediate delays ($\tau_0 \sim 1\,\mathrm{ps}$, green curve) no clear shift is visible. (b) Plot of the peak shift, given by $\tau_0^{\mathrm{eff}} - \tau_0$ where τ_0^{eff} is the delay at which the peak is measured, relative to the τ_0 value along the pulse.

V. SIMULATION DETAILS

In the numerical simulations, we solve the scalar Helmholtz equation $[\Delta + n^2(\vec{r})k^2]\psi(\vec{r}) = 0$ in two dimensions on a regular Cartesian grid via the modular recursive Green's function method [4, 5]. Here, $\Delta = \partial_x^2 + \partial_y^2$ is the Laplacian in two dimensions and $n(\vec{r})$ is the spatially-dependent refractive index distribution with $\vec{r} = (x, y)$ being the position vector. Furthermore, $k = 2\pi/\lambda$ is the free space wave vector and $\psi(\vec{r})$ is the unknown solution.

The scattering system consists of a waveguide with a rectangular, slab-like scattering region (see Fig. S4) of width $W = 1$ and length $L = W/10$ in which circular obstacles of radius $R = W/100$ and refractive index $n_{\mathrm{scat}} = 3.5$ are placed. To match the scattering strength of the experimentally used scattering samples, we use a filling fraction of $f_{\mathrm{scat}} = 0.4$ resulting in an average transmittance of ~ 0.28 (averaged over 10 disorder realizations) and a transport mean free path of $\ell_t \sim 0.31L$ at the central frequency $\omega_0 = 75.55c\pi/W$. We then solve the monochromatic scattering

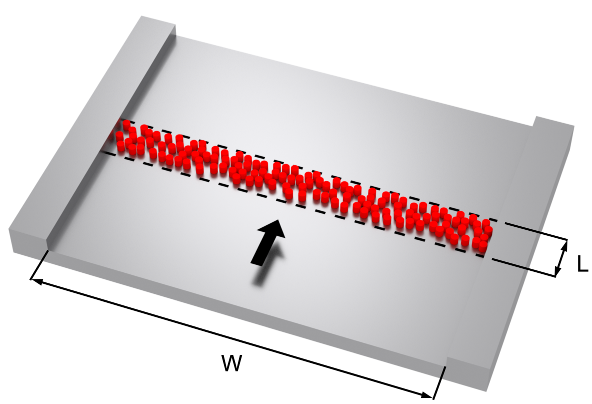

FIG. S4. Sketch of the waveguide setup used in the numerical simulations. The scattering region with width $W = 1$ and length $L = W/10$ (whose boundary is marked by dashed black lines) contains circular obstacles (shown in red) with a radius of $R = W/100$ and refractive index of $n_{\mathrm{scat}} = 3.5$ that fill 40% of its area. The black arrow marks the input side of the system.

problem for 301 frequencies in the interval $\omega \in [50.55, 100.55]c\pi/W$ to obtain the frequency-resolved transmission matrices $T(\omega)$ in the waveguide mode basis.

To arrive at the time-resolved transmission matrices $T(t)$, we Fourier-transform the frequency-resolved transmission matrices and only consider the lowest 50 waveguide modes at the input and output in order to avoid contributions from modes that are evanescent at certain frequencies. Furthermore, we add a spectral function $f(\omega)$ to the Fourier transformation that defines the pulse shape which we choose to be a Gaussian. More precisely, we use $f(\omega) = e^{-(\omega-\omega_0)^2/2\sigma_\omega^2}$ with $\sigma_\omega = \sqrt{2} \times 8/\langle\tau\rangle$. Here, $\langle\tau\rangle = \pi A/C$ is the average time-delay in the scattering medium in two dimensions with $A = LW(1 - f_{\text{scat}}) + LW f_{\text{scat}} n_{\text{scat}}^2$ corresponding to the area of the scattering region (the area of the dielectric scatterers has to be multiplied by their refractive index squared to account for the increased density of states) and $C = 2W$ being the external boundaries through which the waves can enter and exit the system [6, 7].

In analogy to the experiment, we define the temporal origin $\tau = 0$ as the effective time-delay in a homogeneous medium with the same effective refractive index as the scattering medium (see Sec. II). The latter is given by $\tau_{\text{eff}} = L/\langle v_g\rangle$, where $\langle v_g\rangle = (c/n_{\text{eff}})\langle k_x\rangle/\langle k\rangle$ is the mean group velocity with c being the vacuum speed of light and $n_{\text{eff}} = (1-f_{\text{scat}})+f_{\text{scat}}n_{\text{scat}}$ being the homogeneous effective refractive index. Moreover, $\langle k_x\rangle = \langle[\langle k\rangle^2 - k_{y,n}^2]^{1/2}\rangle$ is the mode-averaged longitudinal propagation constant at the mean total wave vector $\langle k\rangle$ and $k_{y,n} = n\pi/W$ are the transverse wave vectors of the waveguide modes. In Fig. 3 of the main text, we use a target time of $\tau_0 = 1.506\langle\tau\rangle$, where the factor 1.506 has been chosen to match the position of the focusing peak with that in the experimental output pulse (at $\tau_0 = 1.1$ ps). All presented results are averaged over 10 disorder realizations with the same parameters.

VI. MINIMAL MODEL TO COMPLEMENT EXPERIMENTAL OBSERVATIONS

A. Simulations

We present the simulation results obtained from a minimal model in which the time-gated TM is regarded as a mere, numerically generated, random matrix (with complex Gaussian independent and identically distributed elements). For this random TM we compute the output fields obtained for different input vectors, the singular modes or the global-focus input, and compare them with experimental observations. In Fig. S5(a), the normalized singular values are compared to the field enhancement obtained in case of phase and amplitude control or phase-only control. The values match well for full control. In case of phase-only control, however, control over the output field is weaker both for increase or decrease, resulting in η_E moving closer to 1. Figure S5(b) shows the evolution of the enhancement for the first singular vector and the global-focus vector with the degree of control γ. As expected from the first singular vector being optimal, its enhancement is always higher than the one obtained for the global-focus. For relatively square TMs (small $1/\gamma$), the effect is clearly visible. The more non-square the TM gets the less difference there is in the observed enhancement. Indeed, in the extreme case of only one non-zero singular value, its associated vector is the same as the global-focus one as there exists only a single output mode. As expected, in the case of phase-only control the observed enhancements decrease.

B. Analytical prediction

Experimentally, as shown in Fig. 4(a) of the main text, and in the simulations presented in Fig. S5 one can observe that the first singular vector gives better enhancement results than the global-focusing input. Here we want to analyse this difference analytically. To do so let us consider a TM T of size $n \times m$ (matrix dimensions given in subscript brackets) and its SVD: $T_{(n,m)} = U_{(n,n)} \times S_{(m,m)} \times V^\dagger_{(m,m)}$. The global-focusing vector $G_{(m,1)}$ is defined such that $G_{(m,1)} = T^\dagger_{(m,n)} I_{(n,1)}$ where the coefficients of I are all unity. Now let us decompose G in the basis of the singular vectors of T,

$$G_{(m,1)} = T^\dagger_{(m,n)} I_{(n,1)} = V_{(m,m)} S^\dagger_{(m,n)} U^\dagger_{(n,n)} I_{(n,1)} = \sum_i^m s_i \sum_j^n u^*_{j,i} V_i, \tag{S5}$$

where s_i are the singular values and $u_{j,i}$ the elements of U. The vector actually displayed on the SLM is normalized such that we have a field at the output E_{G}:

$$\tilde{G} = \frac{G}{||G||_2} = \frac{\sum_i s_i \sum_j u^*_{j,i} V_i}{\sqrt{\sum_i |s_i \sum_j u^*_{j,i}|^2}} \rightarrow E_{\text{G}} = \frac{\sum_i s_i^2 \sum_j u^*_{j,i} U_i}{\sqrt{\sum_i |s_i \sum_j u^*_{j,i}|^2}} \tag{S6}$$

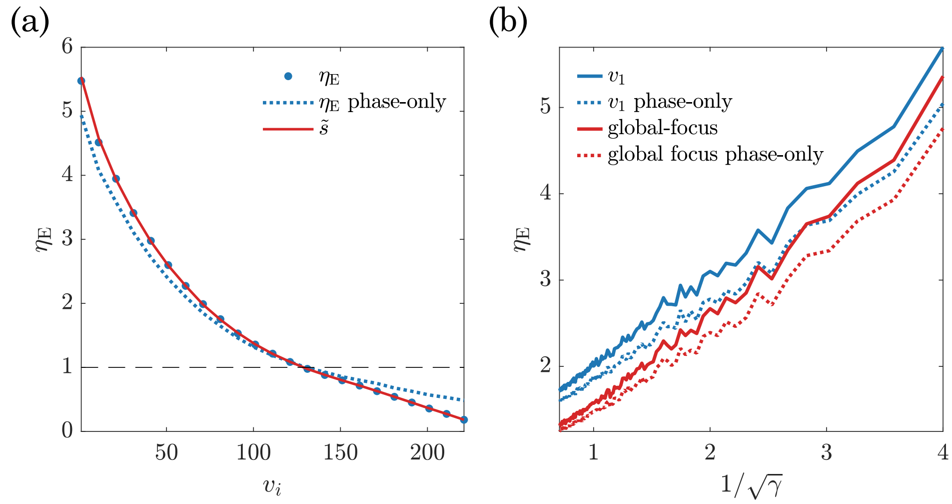

FIG. S5. Minimal model results. (a) Field enhancement values obtained for different singular vectors in case of full control (blue dots) or phase-only control (blue dotted line). These values are plotted together with the normalized singular values $\tilde{s}$ (red line). The simulated TM is of size 1024×225 as for the measurements presented in Fig. 2(a) of the main text. The measured speckle grain size (1.7 pixels) is also accounted for in the simulation (see Supplemental Materials in [8])). The data are averaged over 10 realizations of the disorder. (b) Comparison of the field enhancement values of the first singular vector v_1 (blue) and the global-focusing vector (red) for different degrees of control γ. The full control case is plotted with solid lines while the phase-only case is plotted with dotted lines. As for the experiment presented in Fig. 4(a) of the main text, we vary γ by varying the number of considered pixels in the ROI while keeping the number of SLM modes fixed at 256. Also here the experimental speckle grain size (1 pixel) is accounted for in the simulation. The data are averaged over 10 realizations of the disorder.

Similarly, when sending in a normalized random input $\tilde{R}$ one gets the field $E_{\rm R}$:

$$\tilde{R} = \frac{\sum_i \beta_i V_i}{\sqrt{\sum_i |\beta_i|^2}} \rightarrow E_{\rm R} = \frac{\sum_i s_i \beta_i U_i}{\sqrt{\sum_i |\beta_i|^2}}, \tag{S7}$$

where β_i are the projection coefficients. The total intensity at the output is then

$$I_{\rm R} = E_{\rm R}^\dagger E_{\rm R} = \frac{\sum_i s_i^2 |\beta_i|^2}{\sum_i |\beta_i|^2} \approx \langle s^2 \rangle \text{ (weighted arithmetic mean).} \tag{S8}$$

Note that here the mean is computed over m values. For the global-focusing state, the output intensity is given by the product of two weighted arithmetic means, giving

$$I_{\rm G} = \frac{\sum_i s_i^4 |\sum_j u_{j,i}^*|^2}{\sum_i s_i^2 |\sum_j u_{j,i}^*|^2} \approx \frac{\langle s^4 \rangle}{\langle s^2 \rangle}. \tag{S9}$$

The latter equality is only approximate, as the s_i are not statistically independent from $|\sum_j u_{j,i}^*|$. Nevertheless, it allows for a good approximation of the enhancement which is given by the ratio of the global-focus intensity to the intensity obtained with a random input: $\eta_{\rm I}^{\rm G} = \frac{I_{\rm G}}{I_{\rm R}} = \frac{\langle s^4 \rangle}{\langle s^2 \rangle^2}$. For the SVD the output intensity of the input vector i is more straightforward to compute and is $I_i = s_i^2$, resulting in an enhancement $\eta_{\rm I}^i = \frac{s_i^2}{\langle s^2 \rangle}$. Now let us compare $\eta_{\rm I}^i$ obtained for the i^{th} SVD vector and $\eta_{\rm I}^{\rm G}$,

$$\eta_{\rm I}^{\rm R} = 1 \leq \eta_{\rm I}^{\rm G} = \frac{\langle s^4 \rangle}{\langle s^2 \rangle^2} \leq \eta_{\rm I}^1 = \frac{s_1^2}{\langle s^2 \rangle} = \tilde{s}_1^2. \tag{S10}$$

The first inequality comes from Jensen's theorem and the second from the mean inequality.

In the general, there is no obvious link between the intensity enhancement derived above and the field enhancement, which does not have a simple analytical derivation. However, in case of Rayleigh statistics of the field one can construct this link. One can show that for Rayleigh statistics the ratio of ℓ_1 norms of two vectors is equal to the ratio of the

ℓ_2 norms of these two vectors. Hence, because the amplitude enhancement corresponds to the vectors ℓ_1 norms ratio and the intensity enhancement to the square ℓ_2 norms ratio, one obtains

$$\eta_{\mathrm{E}} \simeq \sqrt{\eta_{\mathrm{I}}} = \tilde{s}. \tag{S11}$$

Note that this property does not hold for the amplitude enhancement of the global-focus due to its Rician statistics (see Sec. VII). Finally, assuming a Marchenko-Pastur distribution, one can expect from Eq. (S10) that the intensity enhancements of the first singular vector scale as $1/\gamma$. For the amplitude enhancements this results in a scaling with $1/\sqrt{\gamma}$ which corresponds well with the experimental observations presented in Fig. 4(a).

VII. SPECKLE STATISTICS

Fully developed speckles are governed by Rayleigh statistics: their amplitude is Rayleigh distributed while their phase distribution is flat. While in the main text we primarily concentrated on the global modulation of the field amplitude at τ_0, here we want to investigate the speckle distribution realized by the different input states. Figure S6 shows that the reference field obtained for a random input as well as the different singular vectors reproduce the Rayleigh statistics (v_1 is shown as an example showing an enhanced average values compared to the reference). However, the global-focusing pattern created by simultaneously focusing on each output pixel results in a Rician distribution of field amplitudes and a preferred phase [9]. This distribution corresponds to the sum of random phasors which have some common component while the Rayleigh distribution corresponds to the sum of fully random phasors. The reason for the emergence of Rician statistics for the global-focus procedure is that it forces a common phase on all targeted output pixels.

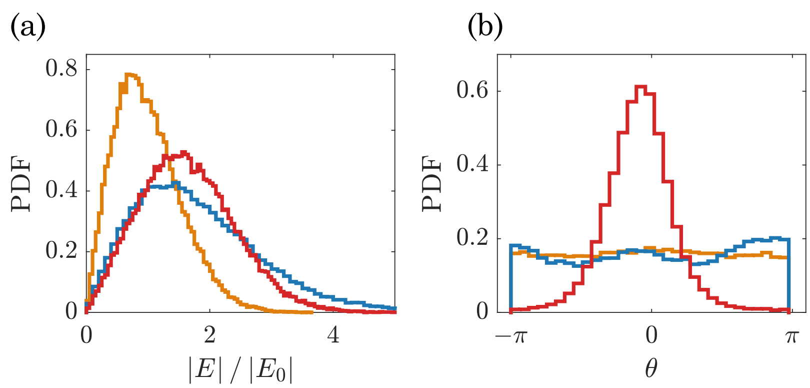

FIG. S6. Speckle statistics. (a) Distribution of field amplitudes for three cases: field obtained from the first singular vector v_1 (blue), field of the global-focusing state (red) and a random reference input (yellow). All three distributions are normalized to the average field amplitude of the random reference E_0. (b) Corresponding phase distributions for the same data.

* louisiane.devaud@lkb.ens.fr

[1] A. Monmayrant, S. Weber, and B. Chatel, A newcomer's guide to ultrashort pulse shaping and characterization, Journal of Physics B: Atomic, Molecular and Optical Physics **43**, 103001 (2010).
[2] M. Davy, Z. Shi, and A. Z. Genack, Focusing through random media: Eigenchannel participation number and intensity correlation, Physical Review B **85**, 035105 (2012).
[3] S. Popoff, G. Lerosey, R. Carminati, M. Fink, A. Boccara, and S. Gigan, Measuring the transmission matrix in optics: an approach to the study and control of light propagation in disordered media, Physical review letters **104**, 100601 (2010).
[4] S. Rotter, J.-Z. Tang, L. Wirtz, J. Trost, and J. Burgdörfer, Modular recursive green's function method for ballistic quantum transport, Phys. Rev. B **62**, 1950 (2000).
[5] F. Libisch, S. Rotter, and J. Burgdörfer, Coherent transport through graphene nanoribbons in the presence of edge disorder, New Journal of Physics **14**, 123006 (2012).
[6] R. Pierrat, P. Ambichl, S. Gigan, A. Haber, R. Carminati, and S. Rotter, Invariance property of wave scattering through disordered media, Proceedings of the National Academy of Sciences **111**, 17765 (2014), https://www.pnas.org/content/111/50/17765.full.pdf.

[7] M. Davy, M. Kühmayer, S. Gigan, and S. Rotter, Mean path length invariance in wave-scattering beyond the diffusive regime, Communications Physics **4**, 85 (2021).
[8] L. Devaud, B. Rauer, J. Melchard, M. Kühmayer, S. Rotter, and S. Gigan, Speckle engineering through singular value decomposition of the transmission matrix, Physical Review Letters **127**, 093903 (2021).
[9] J. Goodman, *Speckle Phenomena in Optics: Theory and Applications* (Roberts & Company, 2007).